ACS NANO

www.acsnano.org

ARTICLE

Strengthening Transition Metal–Oxygen Interaction in Layered Oxide Cathodes for Stable Sodium-Ion Batteries

Junyi Dai,[#] Jiahao Li,[#] Yu Yao,[#] Yan-Ru Wang, Mingze Ma, Ruilin Bai, Yinbo Zhu, Xianhong Rui, Hengan Wu, and Yan Yu*

Cite This: *ACS Nano* 2025, 19, 11197–11209

Read Online

ACCESS | Metrics & More | Article Recommendations | Supporting Information

ABSTRACT: **P2-type layered oxides, such as $Na_{0.67}Ni_{0.33}Mn_{0.67}O_2$, represent a promising class of cathode materials for Sodium-ion batteries (SIBs) due to their high theoretical energy density. However, their cycling stability is often compromised by severe phase transitions and irreversible lattice oxygen redox reactions at high voltages. In this work, we develop a Zn and Al codoping approach to design a $Na_{0.71}Ni_{0.28}Zn_{0.05}Mn_{0.62}Al_{0.05}O_2$ (ZA-NNMO) cathode for stable SIBs. Geometric phase analysis reveals that the introduction of inert Zn significantly mitigates the lattice distortion and transition-metal-ion migration, thereby inhibiting detrimental phase transition and structural collapse. The doped Al element in the Mn site strengthens the Al–O interaction, facilitating reversible O^{2-}–O_2^{n-} ($0 < n < 4$) reactions at high voltages and effectively curtailing irreversible lattice oxygen oxidation, as confirmed by *in situ* differential electrochemical mass spectrometry. As a result, the ZA-NNMO cathode delivers superior electrochemical performance in terms of high output voltage of 3.6 V, highly competitive energy density of 470 W h kg^{-1} and good cyclability (80.2% of capacity retention after 1400 cycles at 1.0 A g^{-1}). This work presents a robust methodology for improving the reversibility and stability of layered oxide cathodes in SIBs.**

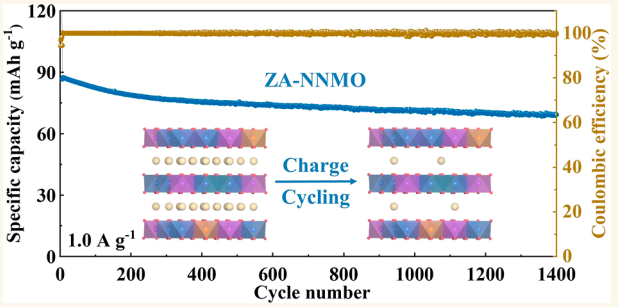

KEYWORDS: *layered oxide, oxygen redox, stable structure, cathode, sodium ion batteries*

Sodium-ion batteries (SIBs) are increasingly recognized as viable alternatives to lithium-ion batteries for large-scale electric energy storage applications, owing to the abundant natural availability of sodium resources.[1−4] However, the energy density of SIBs has not yet fulfilled the increasing requirements of practical applications, largely due to the scarcity of stable and high-capacity cathode materials.[5] Among the recently reported cathode materials, sodium-based layered transition metal oxides (Na_xTMO_2, where TM is a transition metal) emerge as ideal candidates due to their high specific capacity and tap density.[6−12]

Among sodium layered oxides, the water-stable P2-type $Na_{0.67}Ni_{0.33}Mn_{0.67}O_2$ (NNMO) with high ionic conductivity has attracted much attention owing to its elevated working voltage, which arises from both Ni redox ($Ni^{2+} \leftrightarrow Ni^{4+}$) and oxygen redox ($O^{2-} \leftrightarrow O_2^{n-}$) processes.[13] NNMO can deliver a high capacity of about 165 mA h g^{-1} and almost all Na^+ can be deintercalated upon charging to 4.3 V versus Na/Na^+.[14,15] Nevertheless, the NNMO suffers fast capacity decay during the cycling process because of the irreversible phase transformation and oxygen redox.[16,17] The harmful P2−O2 phase transformation derived from the gliding of TM layers can be attributed to the strong O^{2-}–O^{2-} electrostatic repulsion at deep sodium-deintercalation states, resulting in the structure degradation.[18−20] Besides, Na^+ diffusion kinetics in O2 phase is poor; and the oxygen redox reaction is accompanied by irreversible oxygen loss at high voltages above 4.0 V, leading to the capacity decay and voltage fade.[21−23]

Recently, many effective strategies, such as cation doping,[10,24,25] and inert layer coating,[26] have been explored to suppress the dramatic phase transition and irreversible oxygen redox of NNMO. In the case of cation doping, the metal elements like Li,[11] Mg,[25] Cu,[10] Sn,[27] and Ti[24] are used as substitutional elements at redox-active Ni site or electrochemi-

Received: December 21, 2024
Revised: February 25, 2025
Accepted: February 26, 2025
Published: March 11, 2025

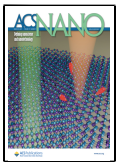

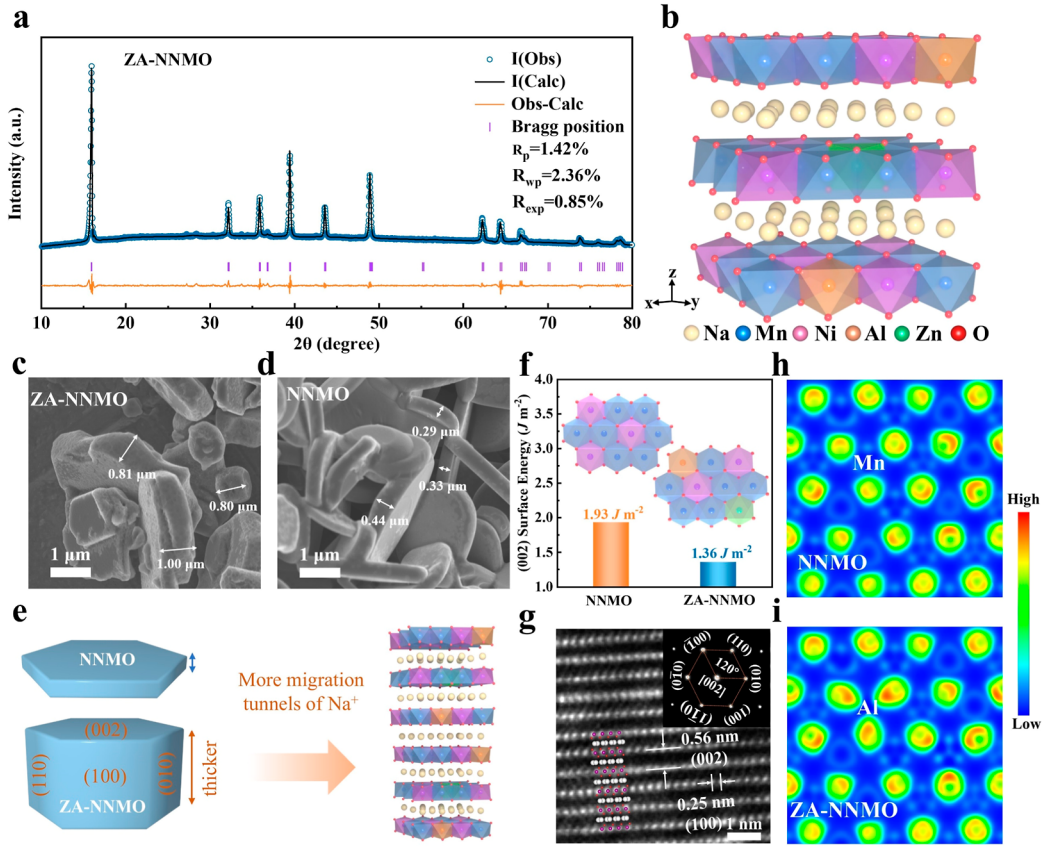

Figure 1. (a) XRD pattern and corresponding Rietveld refinement plot of ZA-NNMO. (b) Schematic crystal structure of ZA-NNMO. SEM images of (c) ZA-NNMO and (d) NNMO. (e) Schematic illustration of NNMO and ZA-NNMO crystal growth with the (002) facet. (f) (002) surface energy of ZA-NNMO and NNMO. (g) HAADF-STEM and corresponding selected-area electron diffraction (SAED) patterns of ZA-NNMO. Electron localization function (ELF) on the (002) plane of (h) NNMO and (i) ZA-NNMO.

cally inert Mn site. For example, substituting Ni with inert Mg and Al can partially suppress the P2−O2 phase transformation,[10,24,25] but issues related to capacity loss due to the reduction of redox-active Ni and irreversible oxygen redox remain unresolved. In addition, substantial research has focused on the modulation of transition metal and oxygen (TM−O) covalency to inhibit the formation of oxygen vacancy and even molecular O_2.[28−30] However, the detrimental phase transition cannot be effectively suppressed simultaneously by modulating TM−O covalency, and the irreversible phase transitions that accumulate during electrochemical cycles eventually result in structural collapse and a decline in electrochemical performance.[31] Therefore, identifying an effective strategy that can simultaneously suppress the harmful phase transition while facilitating a reversible oxygen redox reaction is both challenging and essential for enhancing the electrochemical properties of sodium layered oxide cathodes.

Herein, we propose the partial substitution of Ni and Mn with Zn and Al to develop a $Na_{0.71}Ni_{0.28}Zn_{0.05}Mn_{0.62}Al_{0.05}O_2$ (ZA-NNMO) layered cathode. By substitution of the redox-active Ni with electrochemically inert Zn, the detrimental P2−O2 phase transformation is effectively mitigated. The ZA-NNMO cathode demonstrates P2 phase structural stability and maintains good structural integrity throughout the cycling process. Wavelet transform extended X-ray absorption fine structure (WT-EXAFS) and geometric phase analysis (GPA) reveal that the ZA-NNMO cathode preserves the local Mn environment and reduces lattice distortion such as transition metal migration, thereby enhancing structural stability. The stronger Al−O interactions, as confirmed by *in situ* differential electrochemical mass spectrometry (DEMS), contribute to the suppression of oxygen release and facilitate a reversible O^{2-}−O_2^{n-} oxygen redox reaction within the ZA-NNMO cathode. Density functional theory (DFT) calculations indicate that the oxygen vacancy formation energy of ZA-NNMO is significantly higher than that of NNMO due to the strengthened Al−O interaction, leading to reversible oxygen redox reactions at elevated voltages. By leveraging these advancements, the ZA-NNMO cathode achieves a high energy density of 470 W h kg^{-1} and demonstrates good cyclic stability, with retention rates of 93.4% and 80.2% at 0.1 and 1.0 A g^{-1} over 100 and 1400 cycles, respectively. This work presents a promising strategy for the rational design of advanced layered oxide cathodes utilizing an oxygen-cation-synergistic redox mechanism.

RESULTS AND DISCUSSION

P2-type ZA-NNMO was synthesized by a normal sol−gel method, which is detailed in the Supporting Information. The crystal structure of ZA-NNMO was analyzed by X-ray diffraction (XRD). The Rietveld refinement result (Figure 1a) reveals that ZA-NNMO can be accurately indexed to a hexagonal P2 phase with a space group of $P6_3/mmc$ ($a = b =$ 2.8924 Å, c = 11.1286 Å, $\alpha = \beta = 90°$, $\gamma = 120°$).[32] Detailed atomic positions are presented in Table S1, demonstrating that Zn and Al cations occupy the 2a site without any impurity

https://doi.org/10.1021/acsnano.4c18526
ACS Nano 2025, 19, 11197−11209

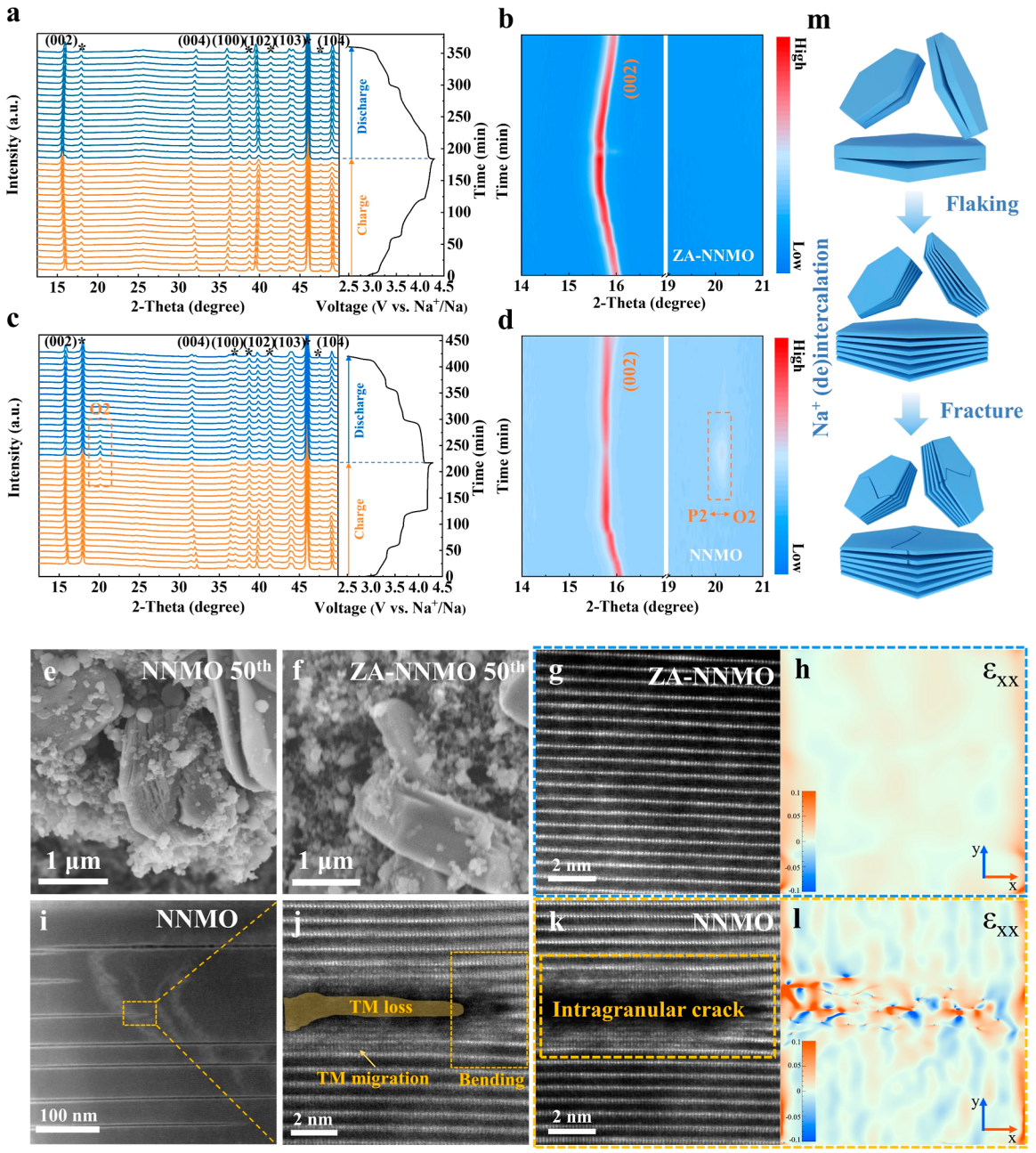

Figure 2. (a) *In situ* XRD patterns of ZA-NNMO and (b) the corresponding intensity contour map during the first cycle. (c) *In situ* XRD patterns of NNMO and (d) the corresponding intensity contour map during the first cycle. SEM images of (e) NNMO and (f) ZA-NNMO after 50 cycles. (g) HAADF-STEM image and (h) corresponding GPA pattern of cycled ZA-NNMO. (i–k) HAADF-STEM images and (l) corresponding GPA pattern of cycled NNMO. (m) Schematic crystal structural collapse of NNMO.

phases. The A-NNMO ($Na_{0.71}Ni_{0.33}Mn_{0.62}Al_{0.05}O_2$) and NNMO cathodes were also synthesized. The XRD patterns and Rietveld refinement results are shown in Figure S1a,b, which similarly correspond to a hexagonal P2 phase with a space group of $P6_3/mmc$. The detailed atomic positions of A-NNMO and NNMO are presented in Tables S2 and S3. The crystal structure of ZA-NNMO is illustrated in Figure 1b. Scanning electron microscopy (SEM) and transmission electron microscopy (TEM) were performed to examine the morphology of the prepared cathode particles. As depicted in Figures 1c,d, and S2, ZA-NNMO shows a flake-like morphology with lateral facets of 1 μm thick, whereas the lateral facets of A-NNMO and NNMO are about 300 nm thick. Interestingly, the crystal growth process of ZA-NNMO microparticles is obviously different, which is that the thickness of the (002) plane of ZA-NNMO is significantly increased. As shown in Figure 1e, more migration tunnels of Na^+ between TMO_2 layers are exposed owning to the thicker (002) plane, which can provide more efficient and direct pathways and accelerate the migration kinetics of the (de)intercalation of Na^+ in a crystal particle.[33,34] To deeply understand the mechanism of crystal growth, DFT calculation of the (002) surface energy was conducted and is summarized in Figures 1f and S3, which includes detailed atomic positions. Obviously, the (002) surface energies of NNMO, A-NNMO, and ZA-NNMO are 1.93, 1.64, and 1.36 J m^{-2}, respectively. This result

https://doi.org/10.1021/acsnano.4c18526
ACS Nano 2025, 19, 11197–11209

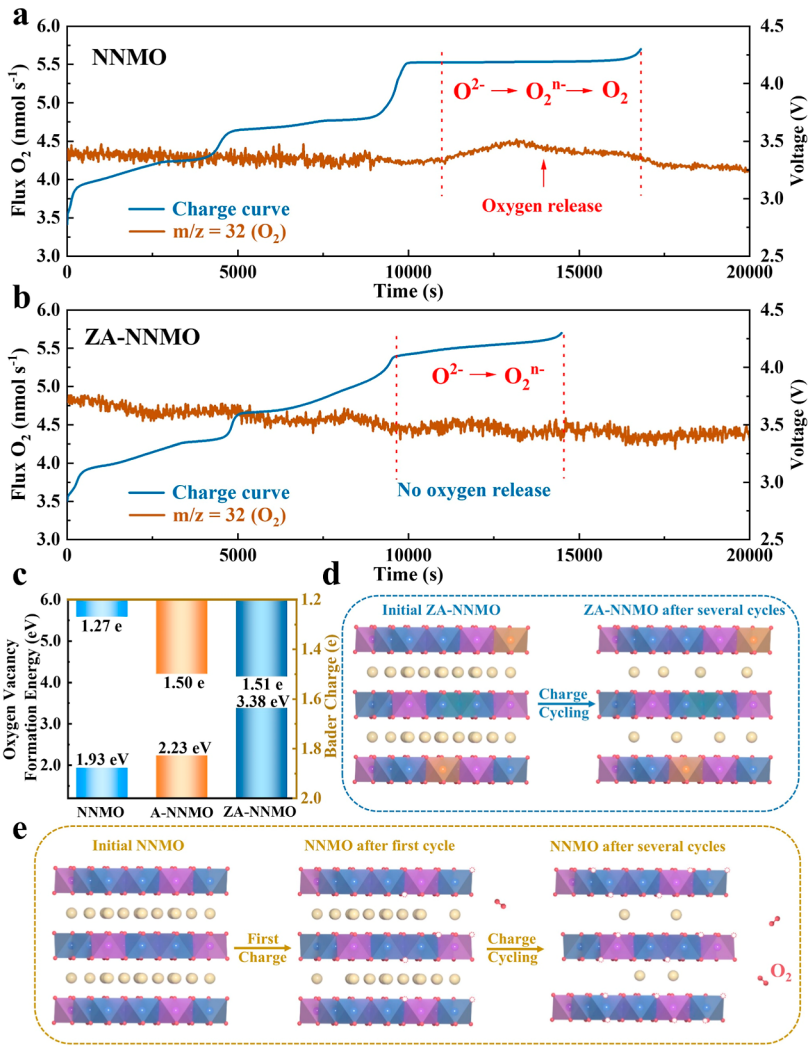

Figure 3. ***In situ*** **DEMS analysis of oxygen evolution during the first charge process for (a) NNMO and (b) ZA-NNMO electrodes. (c) Oxygen vacancy formation energy and charge transfer number of oxygen atoms for NNMO, A-NNMO, and ZA-NNMO. Schematic illustrations of the oxygen redox behaviors for (d) ZA-NNMO and (e) NNMO.**

indicates that the introduction of Zn and Al into TM layers can effectively reduce the (002) surface energy and stabilize the (002) surface, further making the ZA-NNMO microparticles prefer to grow along the (002) crystal plane.[35]

Atomic-level structural characterization of ZA-NNMO was conducted using high-angle annular dark field (HAADF)-spherical aberration corrected scanning transmission electron microscopy (Figure 1g). This analysis reveals a distinct layered arrangement, with interatomic distances of 0.56 and 0.25 nm, corresponding to the *d*-spacing values of the (002) and (100) crystal planes, respectively. Additionally, the diffraction spots observed in the SAED pattern are well indexed, indicating the alignment of transition metals along the [002] direction within a typical hexagonal symmetry phase. Figure S4 shows the HAADF-STEM images and SAED patterns of the A-NNMO and NNMO cathodes. The HAADF-STEM images of A-NNMO and NNMO cathodes exhibit a distinct layered arrangement with interatomic distances of 0.56 nm, corresponding to the *d*-spacing values of the (002) crystal planes (Figure S4a,c). The SAED patterns of A-NNMO and NNMO cathodes can be indexed to a hexagonal P2 phase (Figure S4b,d). It is noted that the superlattice structures were observed in A-NNMO and NNMO cathodes, which are marked in yellow circles in the SAED patterns. The superstructure was not observed in the ZA-NNMO cathode, indicating that the Na^+/vacancy and Ni^{2+}/Mn^{4+} orderings are disrupted, caused by the partial substitution of Ni and Mn with Zn and Al. Energy-dispersive X-ray spectroscopy (EDS) analysis (Figure S5) confirms a homogeneous distribution of all elements within the ZA-NNMO particles. To investigate the impact of doping on the electronic structure, the ELF was analyzed using DFT, as illustrated in Figures 1h,i and S6. Notably, the doping of ZA-NNMO leads to an enhanced Al–O bond, which effectively stabilizes both the lattice oxygen and the crystal structure.[36,37]

The structural stability of cathode materials is crucial to achieving superior electrochemical performance. To assess this stability, *in situ* XRD was employed to monitor the structural evolution of ZA-NNMO and NNMO during charge and discharge cycles within a voltage range of 2.5–4.3 V. Figure 2a,b illustrate the evolution of XRD patterns for ZA-NNMO during the initial charge–discharge cycle. During the first charge, the (002) and (004) peaks progressively shift to lower angles, while the (100) peak shifts to a higher angle. This behavior indicates an increase in lattice parameter *c* and a decrease in lattice parameter *a* due to Na^+ deintercalation. The

https://doi.org/10.1021/acsnano.4c18526
ACS Nano 2025, 19, 11197–11209

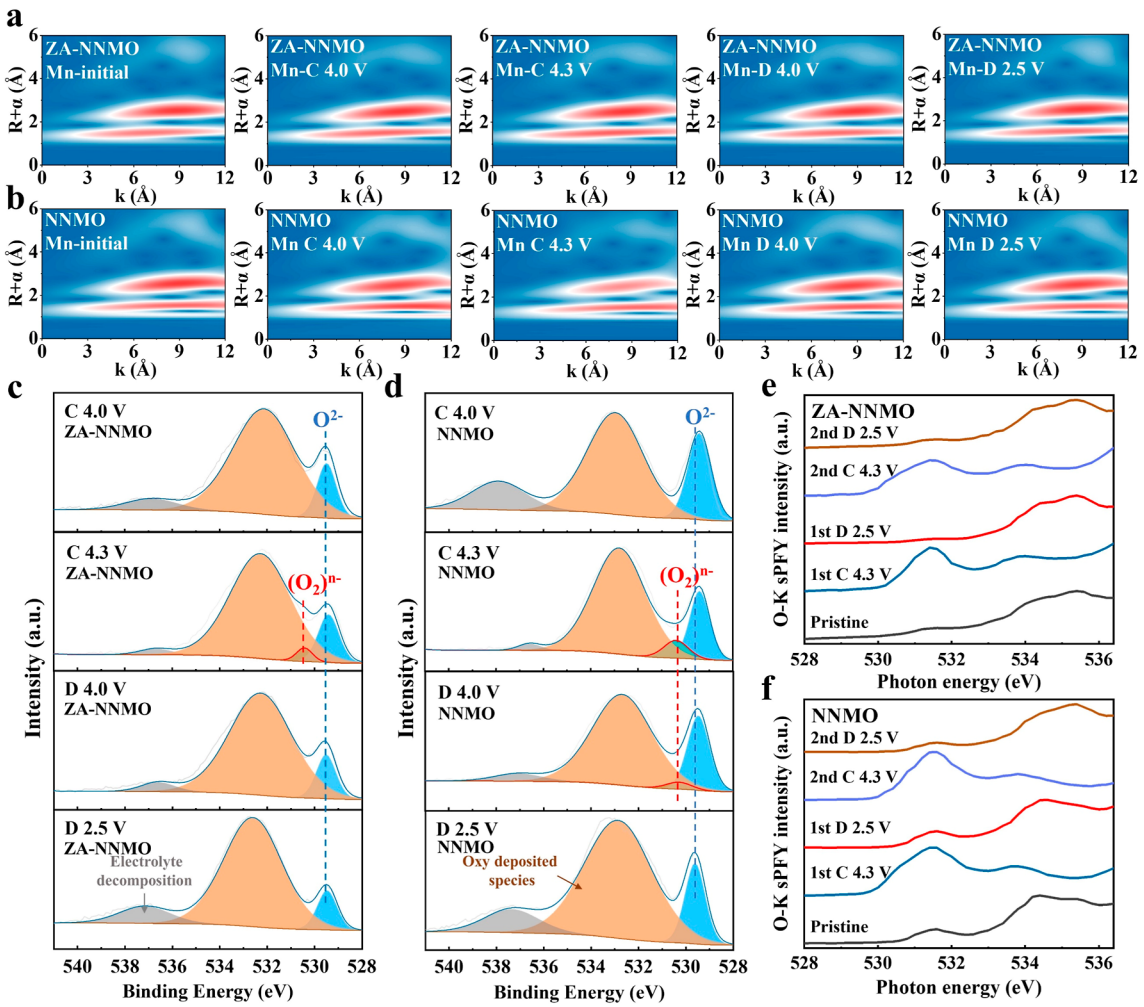

Figure 4. WT-EXAFS spectra of (a) ZA-NNMO and (b) NNMO electrodes at different states of charge and discharge. Ex situ X-ray photoelectron spectroscopy (XPS) analysis for O 1s of (c) ZA-NNMO and (d) NNMO electrodes. *Ex situ* soft X-ray adsorption spectroscopy (XAS) at the O K−edge of (e) ZA-NNMO and (f) NNMO electrodes at different states of charge and discharge.

accompanying stacking graph shows that the primary diffraction peaks continuously shift without the appearance of new peaks beyond the P2 phase, demonstrating the structural stability of ZA-NNMO across the entire voltage range. Furthermore, these peaks shift in opposite directions and return to their original positions during the subsequent discharge, highlighting the highly reversible and sustainable structural evolution of ZA-NNMO throughout the charge−discharge cycle. As for the A-NNMO cathode, the evolution of *in situ* XRD (Figure S7a,b) is largely consistent with that of the ZA-NNMO cathode below 4.2 V. However, it should be noted that the A-NNMO cathode exhibits an O2 structure beyond 4.2 V, indicating that the strong Al−O interaction cannot effectively inhibit the occurrence of detrimental P2−O2 phase transition. In contrast, the undoped NNMO exhibits a clear P2−O2 phase transition beyond 4.2 V (Figure 2c,d).[15] The significant lattice mismatch between the P2 and O2 phases induces substantial stress, leading to rapid capacity degradation.[38,39]

The structure evaluation of ZA-NNMO and NNMO cathodes was further investigated by *ex situ* SEM, STEM-HAADF, and GPA following treatment with focused ion beam scanning electron microscopy under different cycling regimes. SEM images in Figures 2e and S8 reveal significant delamination in the cycled NNMO cathode. This delamination is attributed to the gliding of TMO_2 slabs and the propagation of anisotropic strain, as evidenced by the extensive intergranular and intragranular cracking. These cracks expose the particles to the electrolyte, exacerbating side reactions and ultimately leading to particle pulverization and performance degradation of NNMO.[40] In contrast, the cycled ZA-NNMO cathode maintains its plate-like morphology, as shown in Figures 2f and S8. In order to understand the evolution of microstructures of ZA-NNMO and NNMO cathodes during electrochemical cycles more deeply, HAADF-STEM images were analyzed. Notably, there are no cracks in ZA-NNMO after 50 cycles (Figures 2g and S8). And the atomic arrangement in the bulk of ZA-NNMO maintains the ordered P2-type structure originally observed in Figure 1g, with no apparent lattice distortion or defect, consistent with the uniform strain distribution indicated by the GPA pattern shown in Figure 2h. In contrast, the fractured grains and intragranular cracks are observed on the surface and within the bulk of NNMO (Figures 2i and S8). At high resolution, NNMO displays random lattice distortion and intragranular cracks within the particles (Figure 2j), suggesting transition metal migration, loss, and lattice bending during cycling. The dislocation of TM atoms in NNMO during cycling leads to the

https://doi.org/10.1021/acsnano.4c18526
ACS Nano 2025, 19, 11197−11209

destruction of the original P2-type structural order, accompanied by the inhomogeneous strain in the GPA pattern (Figure 2k,l). The crystal structural collapse diagram of the NNMO is illustrated in Figure 2m. These findings demonstrate that the uneven strain observed in NNMO during electrochemical cycling is mitigated by Zn and Al doping, which maintains the P2 phase structure, as confirmed by *in situ* XRD as shown in Figure 2b. The enhanced structural stability of the ZA-NNMO cathode ensures its superior electrochemical performance.

In addition to investigating the harmful P2−O2 phase transition, it is also imperative to analyze irreversible oxygen loss during electrochemical reactions, which is directly correlated with capacity degradation. To understand this, *in situ* DEMS was utilized to examine the oxygen gas release behavior of NNMO during the charging process (Figure 3a). Upon charging the electrode from its initial state to 4.2 V, no O_2 release was detected. However, a sudden increase in O_2 gas flux is observed between 4.2 and 4.3 V, indicating a notable oxygen loss behavior of NNMO at high voltage. This oxygen loss is thought to be associated with the irreversible evolution of NNMO ($O^{2-}/O_2^{n-}/O_2$).[41] In contrast, *in situ* DEMS analysis of ZA-NNMO (Figure 3b) reveals no detectable O_2 gas throughout the entire charging process, demonstrating the successful suppression of oxygen release at high voltage. This negligible oxygen loss behavior is believed to be linked to the high reversibility (O^{2-}/O_2^{n-}) in ZA-NNMO,[41] highlighting the enhancement of electrochemical reversibility achieved through the mitigation of oxygen release.

To deeply understand this phenomenon, the stability of lattice oxygen was investigated by calculating the oxygen vacancy formation energies for all cathodes. As presented in Figure 3c, the formation energies for ZA-NNMO (3.38 eV) and A-NNMO (2.23 eV) are higher than that of NNMO (1.93 eV), verifying the enhanced lattice oxygen steadiness, in agreement with *in situ* DEMS results. The accumulation of oxygen vacancies can induce a large number of structural defects during electrochemical cycling and eventually result in structure collapse and severe capacity loss of cathode particles.[37] Additionally, the Bader charge analysis was calculated to illustrate the difference in oxygen electron density. The average charge of O atoms in ZA-NNMO and A-NNMO is 1.51 and 1.50 e around Al atoms, respectively, which are more negative than 1.27 e of NNMO, implying the electron localization.[37] The presence of more negative charges around O atoms can effectively suppress the excessive lattice oxygen redox reaction and further irreversible oxygen loss.[37] On the basis of the above analysis, schematic illustrations of the oxygen redox behaviors are presented in Figure 3d,e. Due to the irreversible oxygen loss during the cycling in NNMO cathode, oxygen vacancies are continuously generated and accumulated, which ultimately leads to the TM-O layer slip, structural collapse, and capacity loss. In contrast, ZA-NNMO, with its enhanced lattice oxygen stability, effectively inhibits the formation of oxygen vacancies and subsequent oxygen release. Consequently, ZA-NNMO achieves reversible oxygen redox reactions at high voltages.

Investigating the evolution of atomic local environments is essential for enhancing our understanding of phase transitions and oxygen redox behavior. Wavelet transform (WT) analysis of Mn K-edge spectra was conducted to provide a more intuitive insight into the changes occurring in the surrounding coordination environments of TM, as illustrated in Figure 4a,b. The WT contour plots for ZA-NNMO (Figure 4a) reveal scattering peaks at (6.0 $Å^{-1}$, 1.5 Å) and (9.0 $Å^{-1}$, 2.5 Å), which correspond to the contributions from Mn−O and Mn−TM interactions, respectively.[42] During electrochemical cycling, the peak locations and intensities remain close to their initial states, implying that the coordination environment of Mn in ZA-NNMO remains largely unchanged. In contrast, the intensity of the Mn−TM feature for NNMO is greatly reduced during the charging process, and this intensity does not fully recover to its initial state. These findings, combined with STEM-HAADF and GPA analysis, indicate that NNMO experiences progressive local structural changes, including irreversible TM migration and loss.[43,44] In contrast, ZA-NNMO demonstrated suppressed TM migration.

Additionally, X-ray absorption near edge structure (XANES) analysis reveals a reversible energy shift at the Ni K-edge for both NNMO and ZA-NNMO during charging and discharging processes, whereas no corresponding shift is observed at the Mn K-edge (Figures S9 and S10). This observation suggests that nickel undergoes redox changes; however, these alone cannot fully account for the observed high charge and discharge capacities. It is proposed that lattice oxygen in ZA-NNMO also contributes to charge compensation *via* an anion redox process during these cycles. To further investigate the lattice oxygen redox reaction, the XPS spectra of O element were collected during the charging and discharging processes, as illustrated in Figures 4c,d and S11. For ZA-NNMO, at the initial state and upon charging to 4.0 V (denoted as C 4.0 V), only the peak corresponding to lattice O^{2-} anions (529.5 eV) exists,[41] implying that only the nickel undergoes redox reaction. However, when charged to 4.3 V (denoted as C 4.3 V), an extra O 1s peak emerges at 530.5 eV, which can be attributed to the formation of the O_2^{n-} species.[45−49] This O_2^{n-} peak disappears when discharged to 4.0 V (denoted as D 4.0 V) and subsequently to 2.5 V (denoted as D 2.5 V), indicating that the charge compensation process between 4.0 and 4.3 V is dominated by the O^{2-}/O_2^{n-}. As for NNMO, only the lattice O^{2-} peak at 529.5 eV exists at the initial state and the C 4.0 V state, while the O_2^{n-} peak at 530.5 eV appears when charged to 4.3 V. Notably, upon discharging to 4.0 V, the O_2^{n-} peak persists, ultimately vanishing at the D 2.5 V state. This phenomenon indicates that the oxygen redox kinetic of NNMO is slower than that of ZA-NNMO, which is attributed to the change of the lattice O^{2-} local environment by Zn and Al codoping (Figures 1i and 3c). Additionally, soft XAS at the O K-edge was utilized to probe the electronic structure and local environment of oxygen atoms across various charge/discharge states (Figure 4e,f). The peaks observed between 530.0 and 536.0 eV can be indexed as transition from O 1s to hybridized O 2p−TM 3d states, implying the information on interaction for TM−O.[13] Upon charging to 4.3 V, there is a noticeable enhancement in the peak at 531.6 eV (t_{2g} state) for both ZA-NNMO and NNMO, signifying the occurrence of an oxygen redox process. However, when discharged to 2.5 V during the second cycle, the peak at 534.2 eV (e_g state) for NNMO cannot be restored to its pristine state, contrasting sharply with the good reversibility exhibited by ZA-NNMO. These findings further corroborate the reversible nature of oxygen-involved redox reactions during electrochemical cycling in ZA-NNMO.

In order to demonstrate the advantages of ZA-NNMO, attributed to its stabilized crystal structure and robust chemical bond, the electrochemical performances of ZA-NNMO, A-

https://doi.org/10.1021/acsnano.4c18526
ACS Nano 2025, 19, 11197−11209

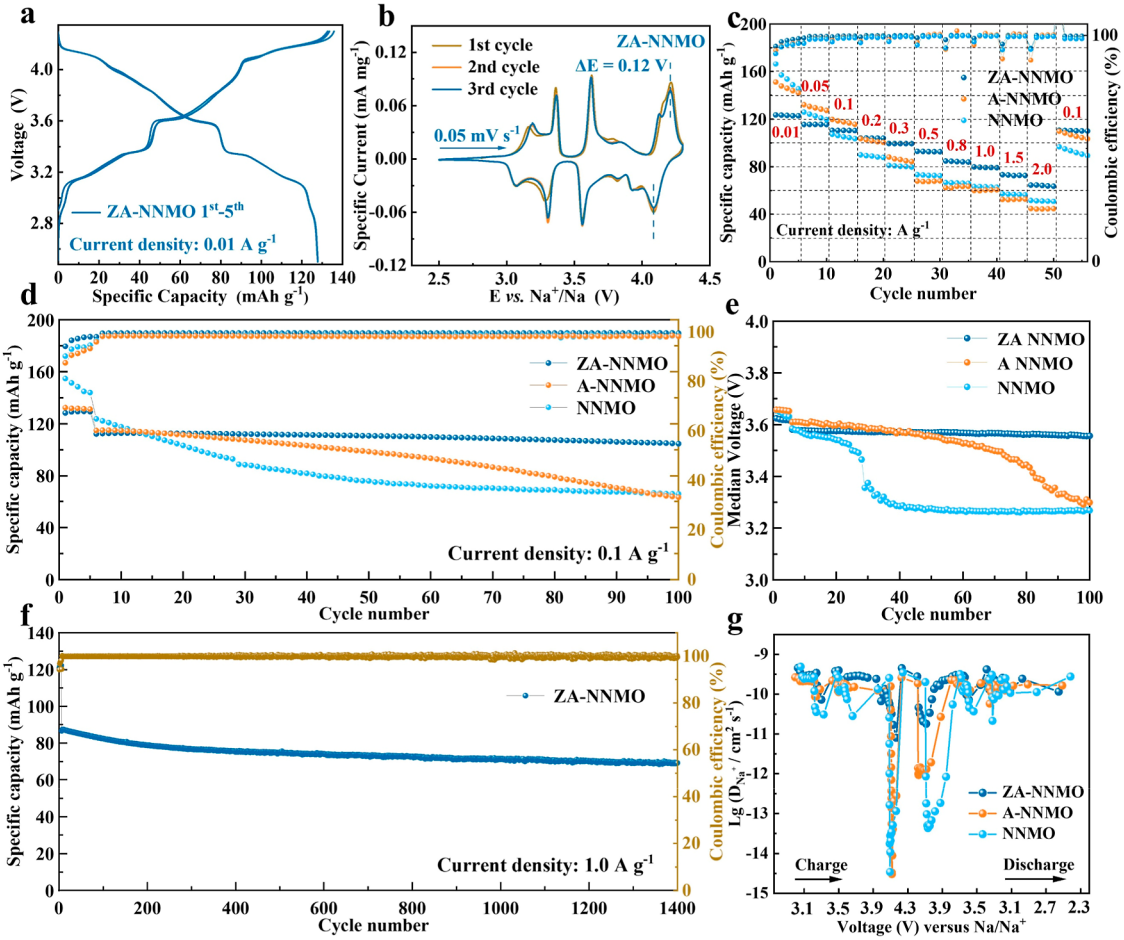

Figure 5. (a) Galvanostatic charge/discharge curves for the first five cycles at a current density of 0.01 A g^{-1} and (b) CV curves for the initial three cycles at a scan rate of 0.05 mV s^{-1} for ZA-NNMO. (c) Rate performance of ZA-NNMO, A-NNMO, and NNMO. (d) Cycling performance and (e) long-term median voltage performance of ZA-NNMO, A-NNMO, and NNMO at 0.1 A g^{-1}. (f) Long-term cycling performance of ZA-NNMO at a high rate of 1.0 A g^{-1}. (g) Calculated Na^+ ions diffusion coefficient of ZA-NNMO, A-NNMO, and NNMO.

NMMO, and NNMO cathodes were measured using sodium half-cells within the voltage range of 2.5−4.3 V (Figure 5). The ZA-NNMO cathode exhibits a high discharge specific capacity of 129.5 mA h g^{-1} and an energy density of 470 W h kg^{-1}, accompanied by an initial Coulombic efficiency of 94.3% at a current density of 0.01 A g^{-1} (Figure 5a). It should be noted that the overlap of the first five galvanostatic charge/discharge curves for ZA-NNMO indicates a stable structural evolution and reversible oxygen redox reactions. In contrast, a rapid capacity loss is observed for the NNMO cathode during the first five cycles at 0.01 A g^{-1} (Figure S12a), which is due to detrimental phase transitions and irreversible oxygen redox processes. Additionally, the A-NNMO cathode shows good electrochemical stability during the first five cycles at 0.01 A g^{-1}, but subsequent cycles display a trend similar to that of the NNMO cathode due to the accumulation of harmful phase transition (Figure S12b). The electrochemical reversibility of these cathodes was further assessed by cyclic voltammetry (CV). For the NNMO cathode (Figure S13a), the CV plot reveals a pair of redox peaks at 4.01 V/4.22 V, corresponding to the oxygen redox couple,[50] showing a bigger polarization voltage of 0.21 V, indicative of slow oxygen redox kinetics. The ZA-NNMO cathode displays a highly reversible electrochemical process, with a pair of redox peaks at 4.09/4.21 V and a smaller polarization voltage of 0.12 V (Figure 5b). The pair of redox peaks of the A-NNMO cathode at 4.06/4.25 V shows a reversible oxygen redox reaction and moderate polarization voltage of 0.19 V (Figure S13b), implying that the dramatic P2−O2 phase transition significantly decelerates the oxygen redox kinetics compared with the ZA-NNMO cathode, which is consistent with the results of dQm/dV curves (Figure S14). Furthermore, this detrimental P2−O2 phase transition, coupled with an uncontrolled oxygen redox reaction resulting from weak interactions between the TM-O, contributes to poor reversibility and severe capacity decay in the NNMO cathode.[51,52] This degradation is further evidenced by the rapid decrease in the intensity of the redox peaks above 4.0 V in the CV plot of the NNMO cathode.

The rate performance of ZA-NNMO, A-NNMO, and NNMO cathodes is compared in Figures 5c and S15. ZA-NNMO cathode exhibits high reversible capacities of 117.3, 111.0, 103.0, 100.0, 91.0, 85.0, 80.0, 75.0, and 65.0 mA h g^{-1} as the current density gradually increases from 0.05 to 2.0 A g^{-1}, respectively. In contrast, the A-NNMO and NNMO cathodes exhibit inferior performance. This disparity is attributed to the superior structural stability and more efficient reversible oxygen redox process in the ZA-NNMO cathode. As shown in Figure 5d, the ZA-NNMO cathode displays a high discharge capacity of 113 mA h g^{-1} with a capacity retention of 93.4% after 100 cycles at 0.1 A g^{-1}. Conversely, the NNMO cathode

https://doi.org/10.1021/acsnano.4c18526
ACS Nano 2025, 19, 11197−11209

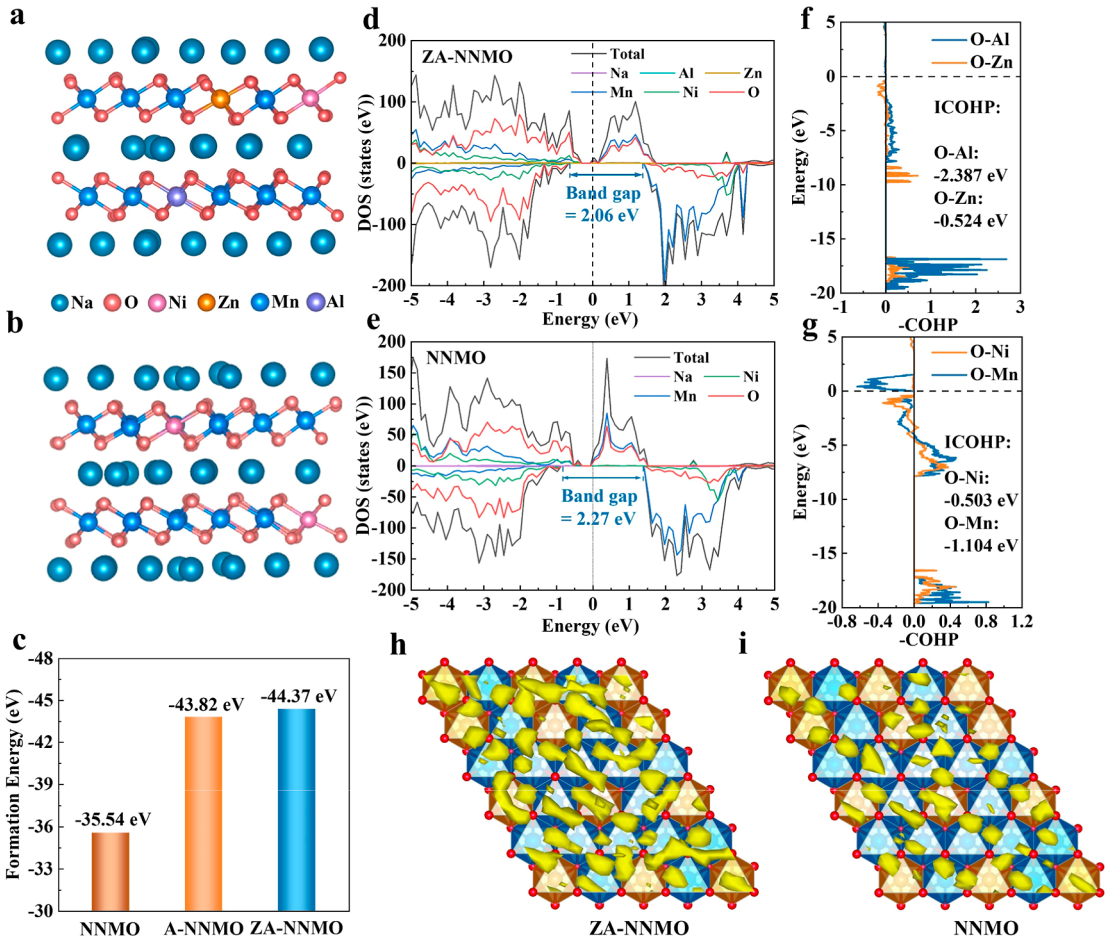

Figure 6. Schematic diagrams of crystal structure along the [002] direction for (a) ZA-NNMO and (b) NNMO. (c) Formation energy of NNMO, A-NNMO, and ZA-NNMO. DOS calculation of (d) ZA-NNMO and (e) NNMO. COHP profiles for (f) O−Zn and O−Al bonds of ZA-NNMO and (g) O−Ni and O−Mn bonds of NNMO. Na^+ diffusion routes in (h) ZA-NNMO and (i) NNMO simulated over a period of 8 ps at a temperature of 700 K.

starts with a capacity of 110.0 mA h g^{-1} but retains only 59.0% after the same number of cycles. The A-NNMO cathode also shows rapid capacity decay after just 30 cycles, primarily due to severe phase transitions that lead to structural degradation. The codoping of Zn and Al can simultaneously inhibit the harmful phase transition and irreversible oxygen loss, which guarantees that the ZA-NNMO cathode exhibits good electrochemical properties. The stability of median discharge voltage during the long cycling process was further evaluated at 0.1 A g^{-1} (Figure 5e). The median voltage of the ZA-NNMO cathode is stable throughout cycling because of the structural stability and reversible oxygen redox reaction. Rapid median voltage decay is observed in A-NNMO and NNMO cathodes, indicating that harmful phase transitions and irreversible oxygen redox reactions can seriously reduce the output voltages, further damaging the energy density of cathodes. Figure S16 shows the charge/discharge curves of ZA-NNMO, A-NNMO, and NNMO cathodes during different cycles. It should be noted that the capacity decay is mainly manifested in the oxygen redox platform above 4.0 V, which confirms that the stable structure and strong TM−O interaction are essential for obtaining a superior electrochemical performance. Even at a high current density of 1.0 A g^{-1}, the ZA-NNMO cathode can deliver a high reversible capacity of 87 mA h g^{-1} with an ultrahigh retention of 80.2% after 1400 cycles (Figures 5f and S17). Furthermore, the Al doping content is increased to 10%, and the cathode does not exhibit a pure hexagonal P2 phase with impurity phases such as Al_2O_3, likely due to the solubility limit (Figure S18). The electrochemical performance of this cathode indicates a significant capacity fade during cycling, which may be attributed to distortion of the initial layered structure.

To investigate the electrochemical kinetics of ZA-NNMO, A-NNMO, and NNMO cathodes, the Na^+ diffusion coefficients (D) were measured by the galvanostatic intermittent titration technique (GITT) (Figures 5g and S19). The Na^+ diffusion coefficients of ZA-NNMO, A-NNMO, and NNMO are similar, in the order of 10^{-9} to 10^{-10} cm^2 s^{-1} when the voltage is below 4.0 V. When the voltage is above 4.0 V, the Na^+ diffusion coefficient of the NNMO cathode displays a rapid decline, ranging from 10^{-13} to 10^{-15} cm^2 s^{-1}, while the Na^+ diffusion coefficient of A-NNMO ranges from 10^{-12} to 10^{-15} cm^2 s^{-1}, indicating that the strong Al−O bond suppresses the irreversible oxygen redox and achieves a stable reaction, especially during the discharging process. However, strong Al−O bond cannot hinder the harmful phase transition at high voltages. The codoping of Zn and Al can make the ZA-NNMO cathode display a higher Na^+ diffusion coefficient of about 10^{-10} cm^2 s^{-1} at high voltages, which is due to the inhibition of irreversible oxygen redox and harmful phase transition. In order to evaluate the influence of electrochemical structural failure on the electrochemical kinetics, the Na^+

https://doi.org/10.1021/acsnano.4c18526
ACS Nano 2025, 19, 11197−11209

diffusion coefficients (D) of NNMO, A-NNMO, and ZA-NNMO cathodes were measured by GITT after 50 cycles (Figures S20 and S21). The Na^+ diffusion coefficients of the NNMO cathode exhibited an obvious decrease after 50 cycles, indicating that the irreversible structural failure of NNMO reduces the diffusion kinetics of Na^+ (Figure S21b). In contrast, the Na^+ diffusion coefficients of the ZA-NNMO cathode showed a further increase after 50 cycles (Figure S21d), which can be attributed to the crystal structural stability of ZA-NNMO and the presence of a conductive cathode/electrolyte interphase that facilitates Na^+ diffusion. Figure S22 shows the activation energies (E) of NNMO, A-NNMO, and ZA-NNMO cathodes at different voltage states of C 4.2, D 4.1, and D 2.5 V after 50 cycles, and the corresponding Nyquist plots at different voltages and temperatures are shown in Figure S23. Obviously, compared with the activation energies of the same cathode at different voltages, the activation energies at C 4.2 V and D 4.1 V are higher than that at D 2.5 V, indicating that the oxygen redox reaction and phase transition occurring at high voltages will greatly reduce the diffusion ability of Na^+. This difference of activation energy is particularly evident in the NNMO cathode, with values of 165.3 kJ mol^{-1} at C 4.2 V, 144.6 kJ mol^{-1} at D 4.1 V and 79.8 kJ mol^{-1} at D 2.5 V. This demonstrates that the introduction of Zn and Al can effectively reduce the activation energy at high voltages, thereby enhancing the Na^+ diffusion kinetics. Furthermore, compared with the activation energies of NNMO, A-NNMO, and ZA-NNMO cathodes at the same voltage state, especially at high voltages, the activation energies of ZA-NNMO (119.5 kJ mol^{-1} at C 4.2 V and 81.9 kJ mol^{-1} at D 4.1 V) and A-NNMO (126.2 kJ mol^{-1} at C 4.2 V and 82.3 kJ mol^{-1} at D 4.1 V) are significantly lower than that of NNMO (165.3 kJ mol^{-1} at C 4.2 V and 144.6 kJ mol^{-1} at D 4.1 V). Based on these advantages, a pouch cell was assembled by ZA-NNMO cathode and hard carbon anode for practical application. The pouch cell delivers a capacity of 1.34 A h within a voltage range of 2.0−4.2 V (Figures S24 and S25). Figure S25a shows the long cycle performance at a current density of 0.5 C with a capacity retention of 89.3% after 100 cycles. The corresponding median discharge voltage remains stable at 3.5 V, without obvious voltage fade during the cycling of the pouch cell (Figure S25b). The detailed parameters for the assembly and electrochemical testing of the pouch full cell are listed in Table S4. Herein, the electrochemical performance of the ZA-NNMO cathode was compared with other recently reported sodium layered oxide cathodes, and the ZA-NNMO cathode exhibits competitive electrochemical performance (Table S5). Overall, the codoping of Zn and Al in NNMO substantially enhances the structural stability and inhibits the irreversible oxidation of lattice oxygen, resulting in good electrochemical performance across the board.

The electronic structures of ZA-NNMO, A-NNMO, and NNMO were studied using first-principles calculations to assess the impact of codoping on their band structures. Their crystal structures are illustrated in Figure 6a,b, and S26. Initial studies focused on thermodynamic stability *via* formation energy analysis. As shown in Figure 6c, the formation energies of ZA-NNMO and A-NNMO are −44.37 and −43.82 eV, respectively, which are much lower than that of NNMO (−35.54 eV). This suggests that the introduction of Al can substantially stabilize the structure, with the most stable configuration achievable during the electrochemical cycle following the codoping of Zn and Al. The density of states (DOS) was calculated to evaluate the electrical conductivity (Figures 6d,e, and S27). The bandgap of ZA-NNMO for the spin-down state is 2.06 eV, which is smaller than that of NNMO (2.27 eV) and A-NNMO (2.23 eV), indicating that codoping with Zn and Al enhances the electronic conduction.[53] To further analyze the effect of doping on bond cohesion strength, the crystal orbital Hamilton populations (COHP) were calculated. As illustrated in Figures 6f,g and S28, the ICOHP value for Mn−O in NNMO is −1.104 eV. After Al doping, this value shifts to −1.741 eV for Al−O in A-NNMO. It is noteworthy that the ICOHP for Al−O in ZA-NNMO is −2.387 eV, indicating a more robust TM−O interaction, thereby reinforcing the electrostatic cohesion within the TM−O layer. These COHP findings essentially confirm the "rivet effect" of Al−O during the oxygen redox process, ultimately facilitating the achievement of reversible oxygen redox reactions. To further understand the impact of codoping on sodium-ion diffusion, ab initio molecular dynamics (AIMD) simulations were conducted. As exhibited in Figures 6h,i, and S29 and S30, the Na^+ probability densities during migration in ZA-NNMO, A-NNMO, and NNMO are presented. The interconnected migration probability densities in ZA-NNMO indicate a higher frequency of Na^+ migrations within the same simulated time frame compared to A-NNMO and NNMO, suggesting improved ion transport dynamics.[54]

CONCLUSIONS

In summary, we have demonstrated that a codoping strategy, replacing Ni with Zn and Mn with Al in $Na_{0.66}Ni_{0.33}Mn_{0.67}O_2$, effectively suppresses the detrimental P2−O2 phase transition and irreversible oxygen release, thereby enhancing the electrochemical performance. The structural stability of ZA-NNMO is notably improved, as evidenced by the stabilization of the P2 phase and a significant reduction in the lattice strain during the cycling. This stability is further corroborated by the maintained local Mn environment and suppression of TM migration, TM loss, and cracking within ZA-NNMO microparticles. The introduction of strong Al−O bonds effectively increases the energy required to form oxygen vacancies, further inhibiting the generation of molecular O_2. Additionally, the reversibility and kinetics of the oxygen redox reactions are enhanced due to the increased charge on the oxygen atoms surrounding Al. These modifications enable ZA-NNMO to deliver a high energy density of 470 W h kg^{-1}, alongside robust cyclic stability of 93.4% after 100 cycles and 80.2% after 1400 cycles at 0.1 and 1.0 A g^{-1}, respectively, without significant voltage fade within the high voltage range of 2.5−4.3 V. Our work emphasizes the significance of synchronously enhancing the structural stability and oxygen redox reversibility in high-performance sodium layered oxide cathodes with oxygen-cation synergetic redox mechanism, which sheds lights on designing advanced sodium layered oxide cathode materials utilizing oxygen redox chemistry for enhanced energy density and cyclic stability.

EXPERIMENTAL SECTION

Chemical and Materials. Sodium acetate trihydrate ($CH_3COONa{\cdot}3H_2O$), nickel acetate tetrahydrate ($Ni(CH_3COO)2{\cdot}4H_2O$), manganese acetate tetrahydrate ($Mn(CH_3COO)2{\cdot}4H_2O$), zinc acetate dihydrate ($Zn(CH_3COO)2{\cdot}2H_2O$), aluminum nitrate nine-water ($Al(NO_3)_3{\cdot}9H_2O$), and citric acid monohydrate ($C_6H_{10}O_8$) were purchased from Aladdin Industrial Corporation. All of the chemicals were used directly without further purification.

https://doi.org/10.1021/acsnano.4c18526
ACS Nano 2025, 19, 11197−11209

Synthesis of ZA-NNMO, A-NNMO, and NNMO Samples. The ZA-NNMO was synthesized *via* a simple sol−gel method. In a typical way, 4.5 mmol of $CH_3COONa{\cdot}3H_2O$ (with a 5 mol % excess), 1.7 mmol of $Ni(CH_3COO)2{\cdot}4H_2O$, 0.3 mmol of $Zn(CH_3COO)2{\cdot}2H_2O$, 0.3 mmol of $Al(NO_3)_3{\cdot}9H_2O$, and 3.7 mmol of $Mn(CH_3COO)2{\cdot}4H_2O$ were dissolved in 25 mL of deionized water containing 2.85 g of citric acid monohydrate. The as-obtained solution was continuously stirred to achieve a transparent solution and then dried under a 60 °C water bath. The obtained gel was dried at 150 °C in an electric oven. Finally, the product of ZA-NNMO was obtained by programmed heating at 500 °C for 6 h, followed by a final treatment at 950 °C for 12 h in a tube furnace under an O_2 atmosphere. The syntheses of A-NNMO and NNMO followed the same procedure as that of ZA-NNMO, with the appropriate stoichiometric ratios.

Material Characterization. The crystal structures of ZA-NNMO, A-NNMO, and NNMO were tested by XRD (Rigaku SmartLab) with a Cu Kα source. The morphologies and microstructures of ZA-NNMO, A-NNMO, and NNMO were characterized *via* TEM (JEM-2100F, JEOL Ltd., Tokyo, Japan). The bonding information was tested by XPS. The crystal structure refinement was carried out using the Rietveld method with full-pattern fitting. The XRD data were refined using the FullProf software, starting from a roughly accurate initial structural model. Parameters such as peak shape, instrument settings, background function, and structural details were iteratively adjusted to obtain a refined structural model that closely matches the experimental data.

Electrochemical Characterizations. The electrodes were fabricated by mixing the active materials (ZA-NNMO, A-NNMO, and NNMO) with carbon black and polyvinylidene difluoride (PVDF) in a mass ratio of 7:2:1, which was then applied onto the carbon-coated Al foil. Then the thin film was dried overnight at 120 °C in a vacuum oven. The loading mass of active materials on the electrodes was 2−3 mg cm^{-2}. Sodium metal foils and glass fiber were used as the counter electrodes and separators, respectively. The electrolyte was 1 M $NaClO_4$ in propylene carbonate with a 5% fluoroethylene carbonate additive. Coin cells (2032-type) were assembled in an argon-filled glovebox with O_2 and H_2O concentrations less than 0.1 ppm. The cycling and rate performances were examined using a Neware battery cycler (BTS BTS-610, Shenzhen, China) within a voltage range of 2.5−4.3 V. A CHI660D electrochemical workstation was used for CV measurement from 2.5 to 4.3 V. *In situ* XRD was conducted by loading the cathode material onto a carbon cloth with a diameter of 12 mm. The loading mass of active materials were approximately 6−8 mg cm^{-2}. *In situ* DEMS was performed by loading the cathode material onto an Al mesh with a diameter of 16 mm. The loading mass of active materials were approximately 6−8 mg cm^{-2}. Sodium metal foils and glass fibers were used as the counter electrodes and separators for both *in situ* XRD and *in situ* DEMS, respectively. The electrolyte was 1 M $NaClO_4$ in propylene carbonate with 5% fluoroethylene carbonate additive.

DFT Calculation. We performed first-principles calculation with the DFT method by the Vienna Ab initio Simulation Package (VASP).[55−57] The projector augmented wave basis set was used to describe the ion−electron interaction, while the GGA + U method was used to describe the d orbitals of transition metals. The applied effective U values given to Mn, Ni, Zn ions were 3.8, 6.1, and 10.0 eV, respectively.[58−60] We used 500 eV as the energy cutoff for the plane-wave basis set, and the force convergence criterion for the relaxation was 0.03 eV $Å^{-1}$. The Gamma scheme *k*-point sampling was used, while 2 × 2 × 2 and 4 × 4 × 4 k-mesh were used for atomic relaxation and DOS calculations, respectively.

The doping formation energy of NNMO, A-NNMO, and ZA-NNMO can be calculated as follows

$$\Delta E_{NNMO} = E(Na_{28}Mn_{28}Ni_{12}O_{80}) - 2E(Mn_{bulk}) - 2E(Ni_{bulk}) - E(Na_{28}Mn_{26}Ni_{10}O_{80})$$

$$\Delta E_{A\text{-}NNMO} = E(Na_{28}Mn_{26}Al_2Ni_{12}O_{80}) - 2E(Al_{bulk}) - 2E(Ni_{bulk}) - E(Na_{28}Mn_{26}Ni_{10}O_{80})$$

$$\Delta E_{ZA\text{-}NNMO} = E(Na_{28}Mn_{26}Al_2Ni_{10}Zn_2O_{80}) - 2E(Al_{bulk}) - 2E(Zn_{bulk}) - E(Na_{28}Mn_{26}Ni_{10}O_{80})$$

where $E(Na_{28}Mn_{28}Ni_{12}O_{80})$, $E(Na_{28}Mn_{26}Al_2Ni_{12}O_{80})$, $E(Na_{28}Mn_{26}Al_2Ni_{10}Zn_2O_{80})$ are the energy of NNMO, ANNMO, ZA-NNMO, respectively, and the subscript bulk means the bulk energy. $E(Na_{28}Mn_{26}Ni_{10}O_{80})$ is the energy before doping.

The vacancy formation energy of O was calculated as

$$\Delta E_{NNMO} = E(Na_{28}Mn_{28}Ni_{12}O_{80}) - 0.5E(O_2) - E(Na_{28}Mn_{28}Ni_{12}O_{79})$$

$$\Delta E_{A\text{-}NNMO} = E(Na_{28}Mn_{26}Al_2Ni_{12}O_{80}) - 0.5E(O_2) - E(Na_{28}Mn_{26}Al_2Ni_{12}O_{79})$$

$$\Delta E_{ZA\text{-}NNMO} = E(Na_{28}Mn_{26}Al_2Ni_{10}Zn_2O_{80}) - 0.5E(O_2) - E(Na_{28}Mn_{26}Al_2Ni_{10}Zn_2O_{79})$$

where $E(Na_{28}Mn_{28}Ni_{12}O_{79})$, $E(Na_{28}Mn_{26}Al_2Ni_{12}O_{79})$, $E(Na_{28}Mn_{26}Al_2Ni_{10}Zn_2O_{79})$ are the energy of NNMO, ANNMO, ZA-NNMO after vacancy formation and $E(O_2)$ is the energy of oxygen.

The diffusion properties of Na ions in NNMO, A-NNMO, and ZA-NNMO were investigated by AIMD calculation.[54,61] We performed AIMD simulations for 8 ps at 700 K by an Andersen thermostat and 1 fs time step, where the only Gamma point was used. The diffusion probability of Na ions was realized by pymatgen-analysis-diffusion code.[62]

COHP[63] was calculated by Lobster and VESTA was used for structure drawing and charge density visualization.[64]

ASSOCIATED CONTENT

Supporting Information

The Supporting Information is available free of charge at https://pubs.acs.org/doi/10.1021/acsnano.4c18526.

Detailed information about XRD patterns and corresponding Rietveld refinement plots of NNMO and A-NNMO; TEM images of ZA-NNMO, A-NNMO, and NNMO; (002) surface energy and ELF on the (002) plane of A-NNMO; HAADF-STEM images and corresponding SAED patterns of A-NNMO and NNMO; EDS of ZA-NNMO; *in situ* XRD patterns and corresponding intensity contour map of A-NNMO; SEM images of NNMO, A-NNMO, and ZA-NNMO after different cycles; charge/discharge curves, CV curves, GITT, Arrhenius plots, Nyquist plots of NNMO, A-NNMO, and ZA-NNMO; XPS analysis, *ex situ* XANES analysis of ZA-NNMO and NNMO; pouch full cell of ZA-NNMO; and DFT calculation of A-NNMO (PDF)

AUTHOR INFORMATION

Corresponding Author

Yan Yu − *Hefei National Research Center for Physical Sciences at the Microscale, Department of Materials Science and Engineering, CAS Key Laboratory of Materials for Energy Conversion, University of Science and Technology of China, Hefei, Anhui 230026, China;* orcid.org/0000-0002-3685-7773; Email: yanyumse@ustc.edu.cn

https://doi.org/10.1021/acsnano.4c18526
ACS Nano 2025, 19, 11197−11209

Authors

Junyi Dai − *Hefei National Research Center for Physical Sciences at the Microscale, Department of Materials Science and Engineering, CAS Key Laboratory of Materials for Energy Conversion, University of Science and Technology of China, Hefei, Anhui 230026, China*

Jiahao Li − *CAS Key Laboratory of Mechanical Behavior and Design of Materials, Department of Modern Mechanics, University of Science and Technology of China, Hefei, Anhui 230027, China*

Yu Yao − *Hefei National Research Center for Physical Sciences at the Microscale, Department of Materials Science and Engineering, CAS Key Laboratory of Materials for Energy Conversion, University of Science and Technology of China, Hefei, Anhui 230026, China*

Yan-Ru Wang − *Instruments Center for Physical Science, University of Science and Technology of China, Hefei, Anhui 230026, China*

Mingze Ma − *Hefei National Research Center for Physical Sciences at the Microscale, Department of Materials Science and Engineering, CAS Key Laboratory of Materials for Energy Conversion, University of Science and Technology of China, Hefei, Anhui 230026, China*

Ruilin Bai − *Hefei National Research Center for Physical Sciences at the Microscale, Department of Materials Science and Engineering, CAS Key Laboratory of Materials for Energy Conversion, University of Science and Technology of China, Hefei, Anhui 230026, China*

Yinbo Zhu − *CAS Key Laboratory of Mechanical Behavior and Design of Materials, Department of Modern Mechanics, University of Science and Technology of China, Hefei, Anhui 230027, China;* orcid.org/0000-0001-9204-9300

Xianhong Rui − *School of Materials and Energy, Guangdong University of Technology, Guangzhou 510006, China;* orcid.org/0000-0003-1125-0905

Hengan Wu − *CAS Key Laboratory of Mechanical Behavior and Design of Materials, Department of Modern Mechanics, University of Science and Technology of China, Hefei, Anhui 230027, China;* orcid.org/0000-0003-0288-1617

Complete contact information is available at: https://pubs.acs.org/10.1021/acsnano.4c18526

Author Contributions

[#]J.D. and J.L. and Y.Y., contributed equally to this work.

Notes

The authors declare no competing financial interest.

ACKNOWLEDGMENTS

J.D., J.L. and Y.Y. contributed equally to this work. This work was supported by the National Natural Science Foundation of China (nos. 51925207, 52394170, 52394171, U24A2067, U24A2064, 52372239, 523B2023, 12232016), the Fundamental Research Funds for the Central Universities (WK9990000170, YD2060002042, WK2090000087), the Liaoning Binhai Laboratory (grant no. LBLF-2023-03), the Strategic Priority Research Program of Chinese Academy of Sciences (grant no. XDA0400202), the State Key Laboratory of Catalysis (no. 2024SKL-B-003), and the Innovation R&D Program of Anhui Province (202423i08050014). The X-ray absorption near edge structure (XANES) of C K-edge was measured by the soft X-ray magnetic circular dichroism end station (XMCD) of National Synchrotron Radiation Laboratory (NSRL). The authors also thank the Shanghai Synchrotron Radiation Facility (BL11B, BL14W1, and BL16B1).

REFERENCES

(1) Armand, M.; Tarascon, J. M. Building better batteries. *Nature* **2008**, *451* (7179), 652−657.

(2) Evarts, E. C. Lithium batteries: To the limits of lithium. *Nature* **2015**, *526* (7575), S93−S95.

(3) Yabuuchi, N.; Kubota, K.; Dahbi, M.; Komaba, S. Research development on sodium-ion batteries. *Chem. Rev.* **2014**, *114* (23), 11636−11682.

(4) Zhao, C.; Wang, Q.; Yao, Z.; Wang, J.; Sanchez-Lengeling, B.; Ding, F.; Qi, X.; Lu, Y.; Bai, X.; Li, B.; et al. Rational design of layered oxide materials for sodium-ion batteries. *Science* **2020**, *370* (6517), 708−711.

(5) Deng, J.; Luo, W. B.; Lu, X.; Yao, Q.; Wang, Z.; Liu, H. K.; Zhou, H.; Dou, S. X. High Energy Density Sodium-Ion Battery with Industrially Feasible and Air-Stable O3-Type Layered Oxide Cathode. *Adv. Energy Mater.* **2018**, *8* (5), 1701610.

(6) Hwang, J. Y.; Myung, S. T.; Sun, Y. K. Sodium-ion batteries: present and future. *Chem. Soc. Rev.* **2017**, *46* (12), 3529.

(7) Liu, Q.; Hu, Z.; Li, W.; Zou, C.; Jin, H.; Wang, S.; Chou, S.; Dou, S.-X. Sodium transition metal oxides: the preferred cathode choice for future sodium-ion batteries? *Energy Environ. Sci.* **2021**, *14* (1), 158−179.

(8) Rong, X.; Xiao, D.; Li, Q.; Niu, Y.; Ding, F.; Hou, X.; Wang, Q.; Xu, J.; Zhao, C.; Zhou, D.; et al. Boosting reversible anionic redox reaction with Li/Cu dual honeycomb centers. *eScience* **2023**, *3* (5), 100159.

(9) Dai, J.; Tan, S.; Wang, L.; Ling, F.; Duan, F.; Ma, M.; Shao, Y.; Rui, X.; Yao, Y.; Hu, E.; et al. High-Voltage Potassium Hexacyanoferrate Cathode via High-Entropy and Potassium Incorporation for Stable Sodium-Ion Batteries. *ACS Nano* **2023**, *17* (21), 20949−20961.

(10) Peng, B.; Chen, Y.; Wang, F.; Sun, Z.; Zhao, L.; Zhang, X.; Wang, W.; Zhang, G. Unusual Site-Selective Doping in Layered Cathode Strengthens Electrostatic Cohesion of Alkali-Metal Layer for Practicable Sodium-Ion Full Cell. *Adv. Mater.* **2022**, *34* (6), No. e2103210.

(11) Wang, Q.; Mariyappan, S.; Rousse, G.; Morozov, A. V.; Porcheron, B.; Dedryvere, R.; Wu, J.; Yang, W.; Zhang, L.; Chakir, M.; et al. Unlocking anionic redox activity in O3-type sodium 3d layered oxides via Li substitution. *Nat. Mater.* **2021**, *20* (3), 353−361.

(12) Wang, K.; Zhang, Z.; Cheng, S.; Han, X.; Fu, J.; Sui, M.; Yan, P. Precipitate-stabilized surface enabling high-performance $Na_{0.67}Ni_{0.33-x}Mn_{0.67}Zn_xO_2$ for sodium-ion battery. *eScience* **2022**, *2* (5), 529−536.

(13) Cheng, C.; Ding, M.; Yan, T.; Jiang, J.; Mao, J.; Feng, X.; Chan, T. S.; Li, N.; Zhang, L. Anionic Redox Activities Boosted by Aluminum Doping in Layered Sodium-Ion Battery Electrode. *Small Methods* **2022**, *6* (3), 2101524.

(14) Lu, Z.; Dahn, J. Intercalation of Water in P2, T2 and O2 Structure $A_z[CoxNi_{1/3-x}Mn_{2/3}]O_2$. *Chem. Mater.* **2001**, *13*, 1252−1257.

(15) Lu, Z.; Dahn, J. R. In Situ X-Ray Diffraction Study of P2-$Na_{2/3}[Ni_{1/3}Mn_{2/3}]O_2$. *J. Electrochem. Soc.* **2001**, *148*, A1225.

(16) Rahman, M. M.; Lin, F. Oxygen Redox Chemistry in Rechargeable Li-Ion and Na-Ion Batteries. *Matter* **2021**, *4* (2), 490−527.

(17) Yang, W. Oxygen release and oxygen redox. *Nat. Energy* **2018**, *3* (8), 619−620.

(18) Lee, D.; Xu, J.; Meng, Y. An advanced cathode for Na-ion batteries with high rate and excellent structural stability. *Phys. Chem. Chem. Phys.* **2013**, *15* (9), 3304−3312.

(19) Wang, P.; You, Y.; Yin, Y.; Wang, Y.; Wan, L.; Gu, L.; Guo, Y. Suppressing the P2−O2 Phase Transition of $Na_{0.67}Mn_{0.67}Ni_{0.33}O_2$ by

Magnesium Substitution for Improved Sodium-Ion Batteries. *Angew. Chem., Int. Ed.* **2016**, *55*, 7445−7449.
(20) Vergnet, J.; Saubanère, M.; Doublet, M.-L.; Tarascon, J.-M. The Structural Stability of P2-Layered Na-Based Electrodes during Anionic Redox. *Joule* **2020**, *4* (2), 420−434.
(21) House, R. A.; Rees, G. J.; McColl, K.; Marie, J.-J.; Garcia-Fernandez, M.; Nag, A.; Zhou, K.-J.; Cassidy, S.; Morgan, B. J.; Saiful Islam, M.; et al. Delocalized electron holes on oxygen in a battery cathode. *Nat. Energy* **2023**, *8* (4), 351−360.
(22) Eum, D.; Kim, B.; Song, J. H.; Park, H.; Jang, H. Y.; Kim, S. J.; Cho, S. P.; Lee, M. H.; Heo, J. H.; Park, J.; et al. Coupling structural evolution and oxygen-redox electrochemistry in layered transition metal oxides. *Nat. Mater.* **2022**, *21* (6), 664−672.
(23) Ren, H.; Li, Y.; Ni, Q.; Bai, Y.; Zhao, H.; Wu, C. Unraveling Anionic Redox for Sodium Layered Oxide Cathodes: Breakthroughs and Perspectives. *Adv. Mater.* **2022**, *34* (8), No. e2106171.
(24) Kubota, K.; Asari, T.; Komaba, S. Impact of Ti and Zn Dual-Substitution in P2 Type $Na_{2/3}Ni_{1/3}Mn_{2/3}O_2$ on Ni-Mn and Na-Vacancy Ordering and Electrochemical Properties. *Adv. Mater.* **2023**, *35* (26), No. e2300714.
(25) Li, Y.; Mazzio, K. A.; Yaqoob, N.; Sun, Y.; Freytag, A. I.; Wong, D.; Schulz, C.; Baran, V.; Mendez, A. S. J.; Schuck, G.; et al. Competing Mechanisms Determine Oxygen Redox in Doped Ni-Mn Based Layered Oxides for Na-Ion Batteries. *Adv. Mater.* **2024**, *36* (18), No. e2309842.
(26) Liu, Y.; Fang, X.; Zhang, A.; Shen, C.; Liu, Q.; Enaya, H. A.; Zhou, C. Layered P2-$Na_{2/3}[Ni_{1/3}Mn_{2/3}]O_2$ as high-voltage cathode for sodium-ion batteries: The capacity decay mechanism and Al_2O_3 surface modification. *Nano Energy* **2016**, *27*, 27−34.
(27) Xiao, Y.; Wang, H. R.; Hu, H. Y.; Zhu, Y. F.; Li, S.; Li, J. Y.; Wu, X. W.; Chou, S. L. Formulating High-Rate and Long-Cycle Heterostructured Layered Oxide Cathodes by Local Chemistry and Orbital Hybridization Modulation for Sodium-Ion Batteries. *Adv. Mater.* **2022**, *34* (33), No. e2202695.
(28) McCalla, E.; Abakumov, A.; Saubanère, M.; Foix, D.; Berg, E.; Rousse, G.; Doublet, M.; Gonbeau, D.; Novák, P.; Van Tendeloo, G.; et al. Visualization of O-O peroxo-like dimers in high-capacity layered oxides for Li-ion batteries. *Science* **2015**, *350* (6267), 1516−1521.
(29) Luo, K.; Roberts, M. R.; Hao, R.; Guerrini, N.; Pickup, D. M.; Liu, Y. S.; Edstrom, K.; Guo, J.; Chadwick, A. V.; Duda, L. C.; et al. Charge-compensation in 3d-transition-metal-oxide intercalation cathodes through the generation of localized electron holes on oxygen. *Nat. Chem.* **2016**, *8* (7), 684−691.
(30) Seo, D. H.; Lee, J.; Urban, A.; Malik, R.; Kang, S.; Ceder, G. The structural and chemical origin of the oxygen redox activity in layered and cation-disordered Li-excess cathode materials. *Nat. Chem.* **2016**, *8* (7), 692−697.
(31) Li, Q.; Xu, S.; Guo, S.; Jiang, K.; Li, X.; Jia, M.; Wang, P.; Zhou, H. A Superlattice-Stabilized Layered Oxide Cathode for Sodium-Ion Batteries. *Adv. Mater.* **2020**, *32* (23), No. e1907936.
(32) Liu, J.; Qi, R.; Zuo, C.; Lin, C.; Zhao, W.; Yang, N.; Li, J.; Lu, J.; Chen, X.; Qiu, J.; et al. Inherent inhibition of oxygen loss by regulating superstructural motifs in anionic redox cathodes. *Nano Energy* **2021**, *88*, 106252.
(33) Ding, F.; Zhao, C.; Xiao, D.; Rong, X.; Wang, H.; Li, Y.; Yang, Y.; Lu, Y.; Hu, Y. S. Using High-Entropy Configuration Strategy to Design Na-Ion Layered Oxide Cathodes with Superior Electrochemical Performance and Thermal Stability. *J. Am. Chem. Soc.* **2022**, *144* (18), 8286−8295.
(34) Fu, F.; Liu, X.; Fu, X.; Chen, H.; Huang, L.; Fan, J.; Le, J.; Wang, Q.; Yang, W.; Ren, Y.; et al. Entropy and crystal-facet modulation of P2-type layered cathodes for long-lasting sodium-based batteries. *Nat. Commun.* **2022**, *13* (1), 2826.
(35) Zhang, Y.; Qiao, R.; Nie, Q.; Zhao, P.; Li, Y.; Hong, Y.; Chen, S.; Li, C.; Sun, B.; Fan, H.; et al. Synergetic regulation of SEI mechanics and crystallographic orientation for stable lithium metal pouch cells. *Nat. Commun.* **2024**, *15* (1), 4454.
(36) Zhang, Q.; Chu, Y.; Wu, J.; Dong, P.; Deng, Q.; Chen, C.; Huang, K.; Yang, C.; Lu, J. Mitigating Planar Gliding in Single-Crystal Nickel-Rich Cathodes through Multifunctional Composite Surface Engineering. *Adv. Energy Mater.* **2024**, *14* (12), 2303764.
(37) Sun, L.; Wu, Z.; Hou, M.; Ni, Y.; Sun, H.; Jiao, P.; Li, H.; Zhang, W.; Zhang, L.; Zhang, K.; et al. Unraveling and suppressing the voltage decay of high-capacity cathode materials for sodium-ion batteries. *Energy Environ. Sci.* **2024**, *17* (1), 210−218.
(38) Somerville, J. W.; Sobkowiak, A.; Tapia-Ruiz, N.; Billaud, J.; Lozano, J. G.; House, R. A.; Gallington, L. C.; Ericsson, T.; Häggström, L.; Roberts, M. R.; et al. Nature of the "Z"-phase in layered Na-ion battery cathodes. *Energy Environ. Sci.* **2019**, *12* (7), 2223−2232.
(39) Zhang, J.-N.; Li, Q.; Ouyang, C.; Yu, X.; Ge, M.; Huang, X.; Hu, E.; Ma, C.; Li, S.; Xiao, R.; et al. Trace doping of multiple elements enables stable battery cycling of $LiCoO_2$ at 4.6 V. *Nat. Energy* **2019**, *4* (7), 594−603.
(40) Gao, S.; Zhu, Z.; Fang, H.; Feng, K.; Zhong, J.; Hou, M.; Guo, Y.; Li, F.; Zhang, W.; Ma, Z.; et al. Regulation of Coordination Chemistry for Ultrastable Layered Oxide Cathode Materials of Sodium-Ion Batteries. *Adv. Mater.* **2024**, *36* (16), No. e2311523.
(41) Zhang, Y.; Wu, M.; Ma, J.; Wei, G.; Ling, Y.; Zhang, R.; Huang, Y. Revisiting the $Na_{2/3}Ni_{1/3}Mn_{2/3}O_2$ Cathode: Oxygen Redox Chemistry and Oxygen Release Suppression. *ACS Cent. Sci.* **2020**, *6* (2), 232−240.
(42) Martini, A.; Signorile, M.; Negri, C.; Kvande, K.; Lomachenko, K. A.; Svelle, S.; Beato, P.; Berlier, G.; Borfecchia, E.; Bordiga, S. EXAFS wavelet transform analysis of Cu-MOR zeolites for the direct methane to methanol conversion. *Phys. Chem. Chem. Phys.* **2020**, *22* (34), 18950−18963.
(43) Lee, G. H.; Lau, V. W. h.; Yang, W.; Kang, Y. M. Utilizing Oxygen Redox in Layered Cathode Materials from Multiscale Perspective. *Adv. Energy Mater.* **2021**, *11* (27), 2003227.
(44) Gent, W. E.; Lim, K.; Liang, Y.; Li, Q.; Barnes, T.; Ahn, S. J.; Stone, K. H.; McIntire, M.; Hong, J.; Song, J. H.; et al. Coupling between oxygen redox and cation migration explains unusual electrochemistry in lithium-rich layered oxides. *Nat. Commun.* **2017**, *8* (1), 2091.
(45) Saubanère, M.; McCalla, E.; Tarascon, J. M.; Doublet, M. L. The intriguing question of anionic redox in high-energy density cathodes for Li-ion batteries. *Energy Environ. Sci.* **2016**, *9* (3), 984−991.
(46) Sathiya, M.; Rousse, G.; Ramesha, K.; Laisa, C. P.; Vezin, H.; Sougrati, M. T.; Doublet, M. L.; Foix, D.; Gonbeau, D.; Walker, W.; et al. Reversible anionic redox chemistry in high-capacity layered-oxide electrodes. *Nat. Mater.* **2013**, *12* (9), 827−835.
(47) Grimaud, A.; Hong, W. T.; Shao-Horn, Y.; Tarascon, J. M. Anionic redox processes for electrochemical devices. *Nat. Mater.* **2016**, *15* (2), 121−126.
(48) Sathiya, M.; Abakumov, A. M.; Foix, D.; Rousse, G.; Ramesha, K.; Saubanere, M.; Doublet, M. L.; Vezin, H.; Laisa, C. P.; Prakash, A. S.; et al. Origin of voltage decay in high-capacity layered oxide electrodes. *Nat. Mater.* **2015**, *14* (2), 230−238.
(49) Pearce, P. E.; Perez, A. J.; Rousse, G.; Saubanere, M.; Batuk, D.; Foix, D.; McCalla, E.; Abakumov, A. M.; Van Tendeloo, G.; Doublet, M. L.; et al. Evidence for anionic redox activity in a tridimensional-ordered Li-rich positive electrode beta-Li_2IrO_3. *Nat. Mater.* **2017**, *16* (5), 580−586.
(50) Zhang, M.; Kitchaev, D. A.; Lebens-Higgins, Z.; Vinckeviciute, J.; Zuba, M.; Reeves, P. J.; Grey, C. P.; Whittingham, M. S.; Piper, L. F. J.; Van der Ven, A.; et al. Pushing the limit of 3d transition metal-based layered oxides that use both cation and anion redox for energy storage. *Nat. Rev. Mater.* **2022**, *7*, 522−540.
(51) Tang, W. H.; Qi, R. Y.; Wu, J. M.; Zuo, Y. Z.; Shi, Y. L.; Liu, R. P.; Yan, W.; Zhang, J. J. Engineering, Understanding, and Optimizing Electrolyte/Anode Interfaces for All-Solid-State Sodium Batteries. *Electrochem. Energy Rev.* **2024**, *7*, 23.
(52) Wu, Y. J.; Shuang, W.; Wang, Y.; Chen, F. Y.; Tang, S. B.; Wu, X. L.; Bai, Z. Y.; Yang, L.; Zhang, J. J. Recent Progress in Sodium-Ion Batteries: Advanced Materials, Reaction Mechanisms and Energy Applications. *Electrochem. Energy Rev.* **2024**, *7*, 17.

https://doi.org/10.1021/acsnano.4c18526
ACS Nano 2025, 19, 11197−11209

(53) Wang, C.; Liu, L.; Zhao, S.; Liu, Y.; Yang, Y.; Yu, H.; Lee, S.; Lee, G. H.; Kang, Y. M.; Liu, R.; et al. Tuning local chemistry of P2 layered-oxide cathode for high energy and long cycles of sodium-ion battery. *Nat. Commun.* **2021**, *12* (1), 2256.
(54) Tapia-Ruiz, N.; Dose, W. M.; Sharma, N.; Chen, H.; Heath, J.; Somerville, J. W.; Maitra, U.; Islam, M. S.; Bruce, P. G. High voltage structural evolution and enhanced Na-ion diffusion in P2-$Na_{2/3}Ni_{1/3-x}Mg_xMn_{2/3}O_2$ ($0 \leq x \leq 0.2$) cathodes from diffraction, electrochemical and ab initio studies. *Energy Environ. Sci.* **2018**, *11* (6), 1470−1479.
(55) Wolverton, C.; Zunger, A. First-Principles Prediction of Vacancy Order-Disorder and Intercalation Battery Voltages in Li_xCoO_2. *Phys. Rev. Lett.* **1998**, *81* (3), 606−609.
(56) Kresse, G.; Hafner, J. Ab initio molecular-dynamics simulation of the liquid-metal-amorphous-semiconductor transition in germanium. *Phys. Rev., B Condens. Matter.* **1994**, *49* (20), 14251−14269.
(57) Kresse, G.; Furthmüller, J. Efficient iterative schemes for ab initio total-energy calculations using a plane-wave basis set. *Phys. Rev. B* **1996**, *54* (20), 11169−11186.
(58) Wang, L.; Maxisch, T.; Ceder, G. Oxidation energies of transition metal oxides within the GGA+U framework. *Phys. Rev. B* **2006**, *73* (19), 195107.
(59) Zheng, W.; Liu, Q.; Wang, Z.; Wu, Z.; Gu, S.; Cao, L.; Zhang, K.; Fransaer, J.; Lu, Z. Oxygen redox activity with small voltage hysteresis in $Na_{0.67}Cu_{0.28}Mn_{0.72}O_2$ for sodium-ion batteries. *Energy Storage Mater.* **2020**, *28*, 300−306.
(60) Harun, K.; Salleh, N. A.; Deghfel, B.; Yaakob, M. K.; Mohamad, A. A. DFT + U calculations for electronic, structural, and optical properties of ZnO wurtzite structure: A review. *Results Phys.* **2020**, *16*, 102829.
(61) Mo, Y.; Ong, S. P.; Ceder, G. First Principles Study of the $Li_{10}GeP_2S_{12}$ Lithium Super Ionic Conductor Material. *Chem. Mater.* **2012**, *24* (1), 15−17.
(62) Deng, Z.; Zhu, Z.; Chu, I.-H.; Ong, S. P. Data-Driven First-Principles Methods for the Study and Design of Alkali Superionic Conductors. *Chem. Mater.* **2017**, *29* (1), 281−288.
(63) Maintz, S.; Deringer, V. L.; Tchougreeff, A. L.; Dronskowski, R. LOBSTER: A tool to extract chemical bonding from plane-wave based DFT. *J. Comput. Chem.* **2016**, *37* (11), 1030−1035.
(64) Momma, K.; Izumi, F. VESTA: a three-dimensional visualization system for electronic and structural analysis. *J. Appl. Crystallogr.* **2008**, *41* (3), 653−658.

https://doi.org/10.1021/acsnano.4c18526
ACS Nano 2025, 19, 11197−11209